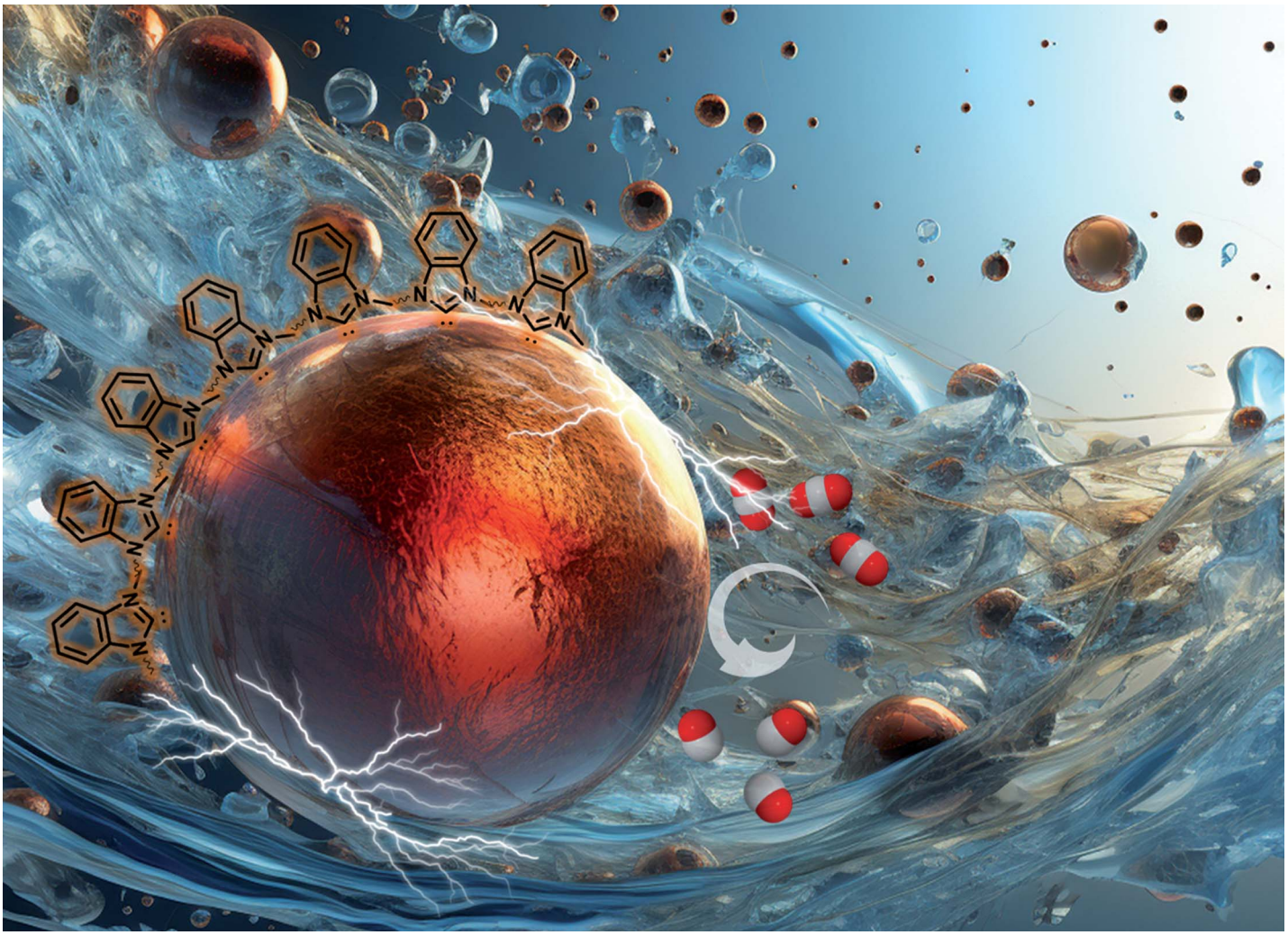

**Showcasing research from Professor Jie He's laboratory at University of Connecticut, Storrs, USA; Professor Shouheng Sun's laboratory at Brown University, Providence, USA; and Professor Peng Bai's laboratory at University of Massachusetts, Amherst, USA.**

Why surface hydrophobicity promotes $CO_2$ electroreduction: a case study of hydrophobic polymer *N*-heterocyclic carbenes

The hydrophobic microenvironment provided by polymer ligands has a profound impact on the hydrogen bonding network of water at the electrolyte-electrode interface. As a result, the hydrophobicity of polymer ligands promotes the clustering of water molecules and enhances the local concentration of $CO_2$ as well as their diffusion within polymer domains, thereby enabling more efficient $CO_2$ reduction.

## As featured in:

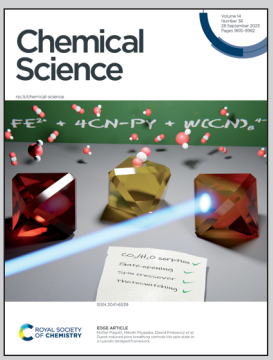


See Peng Bai, Shouheng Sun, Jie He *et al.*, *Chem. Sci.*, 2023, **14**, 9664.

ROYAL SOCIETY OF CHEMISTRY

rsc.li/chemical-science

Registered charity number: 207890

Chemical Science

ROYAL SOCIETY OF CHEMISTRY

EDGE ARTICLE

View Article Online
View Journal | View Issue



Cite this: *Chem. Sci.*, 2023, **14**, 9664

All publication charges for this article have been paid for by the Royal Society of Chemistry



# Why surface hydrophobicity promotes $CO_2$ electroreduction: a case study of hydrophobic polymer *N*-heterocyclic carbenes†

Qiang Luo, [a] Hanyi Duan, [b] Michael C. McLaughlin,[a] Kecheng Wei,[c] Joseph Tapia,[d] Joseph A. Adewuyi,[a] Seth Shuster,[a] Maham Liaqat,[a] Steven L. Suib, [a] Gaël Ung, [a] Peng Bai, *[d] Shouheng Sun *[c] and Jie He *[ab]

We report the use of polymer *N*-heterocyclic carbenes (NHCs) to control the microenvironment surrounding metal nanocatalysts, thereby enhancing their catalytic performance in $CO_2$ electroreduction. Three polymer NHC ligands were designed with different hydrophobicity: hydrophilic poly(ethylene oxide) (PEO–NHC), hydrophobic polystyrene (PS–NHC), and amphiphilic block copolymer (BCP) (PEO-*b*-PS–NHC). All three polymer NHCs exhibited enhanced reactivity of gold nanoparticles (AuNPs) during $CO_2$ electroreduction by suppressing proton reduction. Notably, the incorporation of hydrophobic PS segments in both PS–NHC and PEO-*b*-PS–NHC led to a twofold increase in the partial current density for CO formation, as compared to the hydrophilic PEO–NHC. While polymer ligands did not hinder ion diffusion, their hydrophobicity altered the localized hydrogen bonding structures of water. This was confirmed experimentally and theoretically through attenuated total reflectance surface-enhanced infrared absorption spectroscopy and molecular dynamics simulation, demonstrating improved $CO_2$ diffusion and subsequent reduction in the presence of hydrophobic polymers. Furthermore, NHCs exhibited reasonable stability under reductive conditions, preserving the structural integrity of AuNPs, unlike thiol-ended polymers. The combination of NHC binding motifs with hydrophobic polymers provides valuable insights into controlling the microenvironment of metal nanocatalysts, offering a bioinspired strategy for the design of artificial metalloenzymes.

Received 25th May 2023
Accepted 31st July 2023

DOI: 10.1039/d3sc02658b

rsc.li/chemical-science

## 1. Introduction

There have been rising concerns on practicality and sustainability of catalysts for $CO_2$ electroreduction. Metal nanocatalysts, particularly those made of precious metals, can have high initial activity for $CO_2$ activation;[1–3] but, they are unstable under redox conditions, which leads to a fast activity decay. For example, gold nanoparticles (AuNPs) are among the most active catalysts to reduce $CO_2$ to CO.[4–7] Even with the most stable nanostructures as nanospheres, AuNPs showed fast morphological evolution in the course of electrochemical $CO_2$ reduction, *e.g.*, growing into large, branched structures mainly through interparticle coalescence by the random walking of AuNPs.[8,9] This uncontrolled sintering of AuNPs reduces the catalyst active sites and lower the catalytic selectivity towards $CO_2$.[10] Even more serious sintering behaviors seen in copper (Cu),[10–12] silver (Ag)[13] and palladium (Pd)[14] catalysts during the $CO_2$ electroreduction process. It cannot be overstated that, for applications, a reasonable lifespan of nanocatalysts for $CO_2$ reduction is a must to decrease the overall cost of electrolysis. Another important aspect of $CO_2$ electroreduction is their selectivity. As the $CO_2$ reduction process involves the proton-coupled electron transfer, proton reduction often competes with $CO_2$ reduction.[15] For example, commercial polycrystalline Cu foil has a selectivity of only ~50% to reduce $CO_2$ at −0.8 V [16,17] (*vs.* reversible hydrogen electrode, RHE, the same hereafter) and commercial Pd/C shows a selectivity of ~40% to reduce $CO_2$ at −0.6 V.[9,18,19] A high selectivity of $CO_2$ over protons would increase the faradaic efficiency (FE) of the input electrical energy toward the formation of carbonous products.

A number of methods have been reported to improve the catalyst stability and selectivity for $CO_2$ electroreduction, *e.g.*, strong metal–support interaction,[20–22] and polycrystalline metal–oxide interface.[23–25] Among these approaches, the

[a]*Department of Chemistry, University of Connecticut, Storrs, CT 06269, USA. E-mail: jie.he@uconn.edu*

[b]*Polymer Program, Institute of Materials Science, University of Connecticut, Storrs, CT 06269, USA*

[c]*Department of Chemistry, Brown University, Providence, Rhode Island 02912, USA. E-mail: ssun@brown.edu*

[d]*Department of Chemical Engineering, University of Massachusetts, Amherst, Massachusetts 01003, USA. E-mail: pengbai@umass.edu*

† Electronic supplementary information (ESI) available: Additional polymer synthesis procedures with NMR, TGA, XPS, surface modification, $CO_2$ electroreduction catalysis results, simulation, TEM, and ATR-SEIRAS spectra. See DOI: https://doi.org/10.1039/d3sc02658b

incorporation of rationally designed surface ligands on nanocatalysts has attracted much attention recently.[26–35] As inspired by metalloenzymes where the stability and overall efficiency of the active metal sites rely on finely engineered protein frameworks, passive organic ligands anchored to the surface of nanocatalysts can stabilize nanocatalysts and simultaneously provide a similar microenvironment that controls the selectivity for $CO_2$ electroreduction.[27,36] Ligands at the catalyst–electrolyte interface where the reduction normally occurs control how substrates bind/activate on the catalyst and/or stabilize key rection intermediates, simultaneously preventing the interparticle coalescence.[27] In case of Cu nanocatalysts, the use of hydrophobic polymers like perfluorinated sulfonic acid (PFSA) ionomers improves the selectivity for $CO_2$ reduction, *e.g.*, 65–75% to ethylene at a peak partial current density of 1.34 A $cm^{-2}$.[37] The hydrophobic $(CF_2)_n$ domains on the surface of Cu provided continuous percolating hydrophobic paths for the diffusion of gas reactants to improve the selectivity for $CO_2$ reduction while stabilizing Cu catalysts up to 60 h. Other hydrophobic organic ligands like 1-octadecanethiol could yield superhydrophobic Cu dendrites that largely suppress the proton reduction, although some of those non-conductive ligands were detrimental to the activity of nanocatalysts.[38] Alternatively, stable carbenes, like *N*-heterocyclic carbenes (NHCs), have been widely used as organic ligands for a variety of transition metals including their NPs.[39–42] NHC–metal coordination is not redox active, as compared to metal–thiolate; therefore, it provides excellent stability to metal nanocatalysts under $CO_2$ reduction conditions. The strong σ-electron substituent effect also enriches the surface electron density of metals that facilitates the binding of electrophilic $CO_2$. For example, NHC ligands could promote the activity of Pd foil by 32-fold with a high selectivity to formate (86%).[43] In addition to enhanced activity, the redox-inactive Pd–C coordination could significantly improve the stability of Pd. In combination of NHCs as the strong binding motif and organic polymers with desired functionality (*e.g.*, hydrophobicity), polymer NHC ligands have profound impact on the catalytic reactivity of metal nanocatalysts for $CO_2$ reduction. As a surface coating to metal nanocatalysts, polymer NHCs can control the accessibility of substrates at the catalyst–electrolyte interface,[36] simultaneously improving the long-term stability of metal nanocatalysts.

In the present study, we aim to articulate the synergetic effect of polymer hydrophobicity and NHCs in addressing three fundamental questions regarding the significance of localized hydrophobicity, the diffusive characteristics of substrates, and the stability of metal–NHC binding. We examined three NHC-terminated polymers, namely poly(ethylene oxide) (PEO), polystyrene (PS), and the block copolymer (BCP) of PEO-*b*-PS, as ligands to control the catalytic efficiency of $CO_2$ electroreduction for gold nanoparticles (AuNPs) (as shown in Scheme 1). Our key findings are threefold. Firstly, regardless of the hydrophobicity of the polymer, NHCs, as a binding motif, can suppress proton reduction. We used a molecular probe, 1-butyl-3-methyl-1*H*-benzimidazolium bromide (BMB–Im), to demonstrate that the partial current attributed to hydrogen is

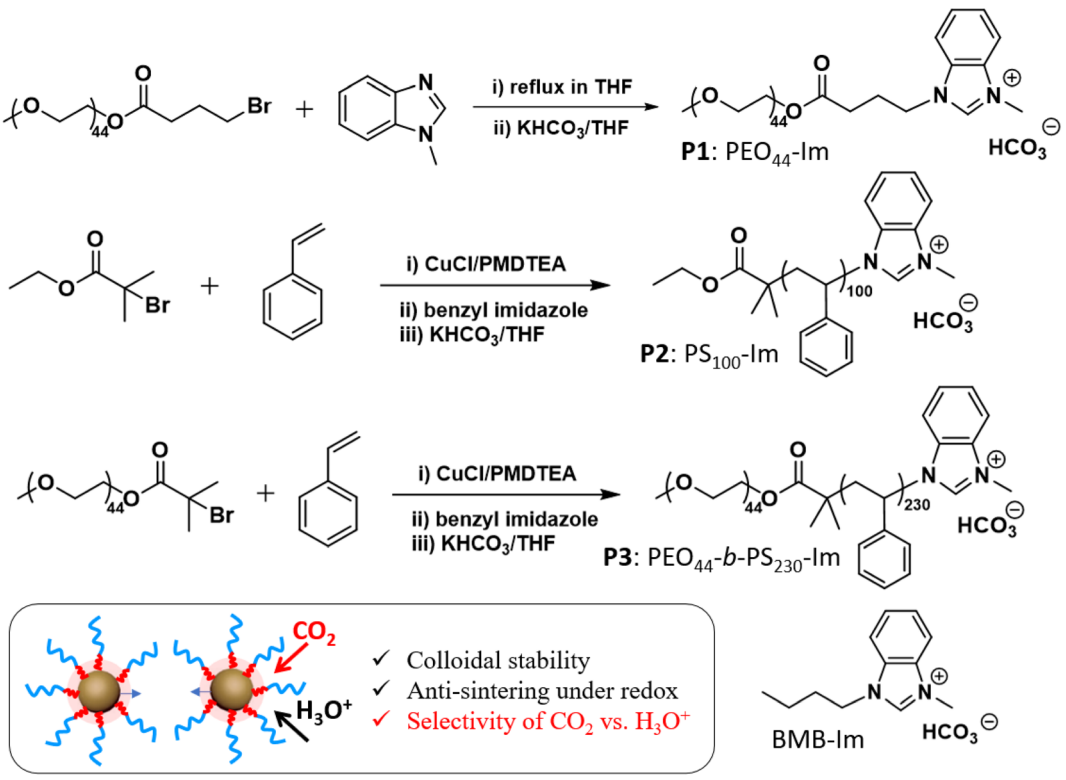


Scheme 1 Synthesis of three Im-terminated polymer ligands, including $PEO_{44}$–Im (P1), $PS_{100}$–Im (P2), $PEO_{44}$-*b*-$PS_{230}$–Im (P3), and molecular BMB–Im.

independent of the polymer environment or their hydrophobicity. Secondly, polymer ligands incorporating hydrophobic PS segments, such as homopolymer PS and PEO-*b*-PS, exhibited a twofold increase in the partial current density for CO formation compared to the hydrophilic PEO. Hydrophobic polymers enhanced the selectivity for $CO_2$ reduction in the potential range of −0.7 to −1.1 V, with a CO FE of 90–95%. Our results strongly indicate that the diffusion of ions was not hindered by any of the polymers. From a mechanistic perspective, the hydrophobicity of the polymers affected the localized hydrogen bonding network of water, as confirmed by attenuated total reflectance surface-enhanced infrared absorption spectroscopy (ATR-SEIRAS) and molecular dynamic simulation. This hydrophobicity-induced structural change of water likely contributed to the observed enhancement in selectivity for $CO_2$ reduction. Lastly, polymer NHC ligands also provided stability to AuNPs under reductive potential. By employing ATR-SEIRAS, we analyzed the detachment mechanism of these NHC ligands, comparing them to polymer thiol ligands. The strong interaction between hydrophobic polymers and AuNPs presents a stable microenvironment that promotes $CO_2$ reactivity at the interface, thus representing a potential avenue for mimicking such behavior of metalloenzymes.

## 2. Results and discussion

Three different polymer methylbenzimidazolium salts with bicarbonate counter ions were used as polymer NHC precursors (see ESI† for synthetic details). The first polymer, methylbenzimidazolium-terminated PEO (P1, $PEO_{44}$–Im, $M_n$ 2 kg $mol^{-1}$), was prepared through the esterification of monohydroxy PEO with 4-bromobutyric acid and further alkylation with 1-methylbenzimidazole (Scheme 1). Methylbenzimidazolium-terminated polystyrene (P2, $PS_{100}$–Im, $M_n$ 10.7 kg $mol^{-1}$, $Đ = 1.14$) and the amphiphilic BCP (P3, $PEO_{44}$-*b*-$PS_{230}$–Im, $M_n$ 27.0 kg $mol^{-1}$, $Đ = 1.18$) were synthesized from atom transfer radical polymerization (ATRP). The end halide group was further converted through the alkylation with 1-methylbenzimidazole under reflexing in *N*,*N*-dimethylformamide with trace amount of KI as the catalysts, similarly to our previous reports.[44–46] The same alkylation procedures were carried out for $PEO_{44}$–Im (P1), $PS_{100}$–Im (P2), $PEO_{44}$-*b*-$PS_{230}$–Im (P3) and 1-butyl-3-methyl-1*H*-benzimidazolium bromide (BMB–Im). The halide ions were further exchanged with excess $KHCO_3$ in tetrahydrofuran (THF) (Scheme 1). To remove the residual KCl, the polymer solution was purified by passing through a silica gel column twice. The final product of three polymers was obtained by precipitation and dried under vacuum. The BMB–Im was used for surface modification directly in the solution of $KHCO_3$ as described below. The characterization details are summarized in ESI (Fig. S1–S4†).

AuNPs (diameter 14 ± 1.7 nm, Fig. S15†) were synthesized and modified by polymer NHCs through a "grafting to" method as reported previously.[36,46] To ensure the ohmic contact between AuNPs and the electrode, citrate-capped AuNPs were first adsorbed on activated carbon (Printex U, *ca.* 50 nm nanospheres). Typically, 30 mg of activated carbon was dispersed in 10 mL of ethanol and further mixed with the stock solution of AuNPs (120 mL in water with a concentration of 0.1 mg $mL^{-1}$). After stirring overnight, Au/C (~40 wt% Au) catalysts powder was collected by centrifugation. Au/C catalysts were further modified with polymer ligands in THF (see details in ESI†). Au/C catalysts modified by BMB–Im was carried out in 0.1 M of $NaHCO_3$ solution containing BMB–Im. The unbound ligands were removed through two centrifugation cycles. The surface grafting was first confirmed by Fourier-transform infrared spectroscopy (FT-IR) (Fig. S5†). For example, $PS_{100}$–Im shows typical aromatic C–H stretching at 3025 $cm^{-1}$, aliphatic C–H stretching at 2916 (as) and 2814 (s) $cm^{-1}$ and aromatic ring breathing mode at 1600–1400 $cm^{-1}$. Similar vibrational peaks were observed for PS-grafted Au/C catalyst. The formation of NHC on the surface of AuNPs was examined by X-ray photoelectron spectroscopy (XPS, Fig. S6†). In case of BMB–Im, a well-resolved N 1s peak at 400.2 eV was seen for Au/C grafted by BMB–Im, characteristic for the conversion of the charged benzimidazolium to benzimidazole NHC.[47,48] The grafting density of ligands was measured by thermogravimetric analysis through the weight loss of polymer ligands (Fig. S7†). The grafting density is 1.2 chains per $nm^2$ for P1, 0.8 chains per $nm^2$ for P2, and 0.6 chains per $nm^2$ for P3, respectively. While all three polymers showed reasonably high grafting density, P1 had a slightly higher grafting density, due to its low molecular weight.

To quantify the accessibility of Au catalysts after surface modification with NHC ligands, electrochemically active surface area (ECSA) of AuNPs were examined using cyclic voltammetry (CV, Fig. 1a). The typical CVs were measured in 0.5 M $H_2SO_4$ saturated with $N_2$ a scan rate of 100 mV $s^{-1}$. In the cathodic scan, the reduction peak was seen at 1.15 V *vs.* RHE, assigned to the reduction of surface oxygenated monolayer. The peak area is proportional to the electrochemically active surface.[49] In the absence of ligands, as shown in Fig. 1b, Au/C shows an ECSA of 0.25 ± 0.01 $cm^2$ $\mu g^{-1}$. With hydrophilic PEO–NHC, Au–P1 has a minimum change of its ECSA of 0.23 ± 0.001 $cm^2$ $\mu g^{-1}$. Hydrophobic PS, on the other hand, decreases the accessibility of Au. Au–P2 and Au–P3 have an ECSA of 0.14 ± 0.01 and 0.13 ± 0.01 $cm^2$ $\mu g^{-1}$, respectively. The CVs in 0.1 M $KHCO_3$ are given in Fig. 1c and d. Under $N_2$, a similar catalytic reduction for Au/C and Au–P3/C was observed. For Au–P3, there was an increase of its current density under $CO_2$, indicating its high selectivity toward $CO_2$ as compared to that of Au/C. Similar trend could be observed for Au–P1 and Au–P2 (Fig. S8†). The typical linear sweep voltammograms (LSVs) are displayed in Fig. 1e (normalized to geometric electrode surface area) and Fig. 1f (normalized to ECSA). Interestingly, all polymer NHCs modified Au catalysts showed higher activity than Au/C. The positive shift of the onset potentials and the increase of current density were more obvious when considering the intrinsic activity of AuNPs as shown in Fig. 1f.

More quantitatively, the electrocatalytic activity and selectivity of all catalysts were further analyzed through faradaic efficiency (FE) and their partial current density toward CO ($J_{CO}$) and $H_2$ ($J_{H_2}$). Electrocatalytic $CO_2$ reduction was carried out in a custom-made H cell separated with a Nafion membrane using

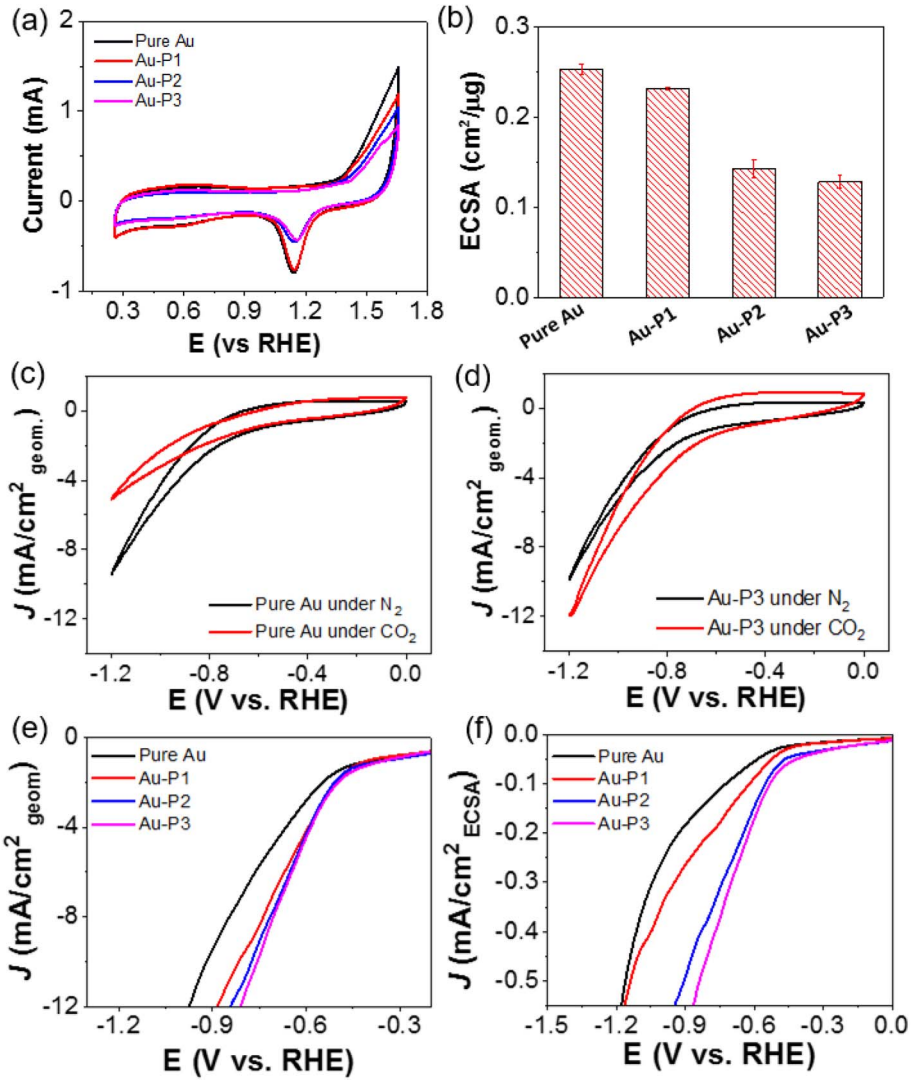


Fig. 1 (a) CVs of Au/C with different polymer ligands measured in $N_2$-saturated 0.5 M $H_2SO_4$ with a scan rate of 100 mV $s^{-1}$. (b) ECSAs of AuNPs modified with various ligands. (c) and (d) CV curves of AuNPs (c) and Au–P3 (d) under $N_2$ (black) and $CO_2$ (red). (e) and (f) LSV curves measured in $CO_2$-saturated 0.1 M $KHCO_3$ at a scan rate of 10 mV $s^{-1}$ normalized to (e) geometric area of electrodes and (f) ECSA of AuNPs.

0.1 M $KHCO_3$ as a supporting electrolyte. Au/C without NHC ligands yielded CO with FE of 64 to 76% in the potential range of −0.7 to −1.1 V. Those CO FE values are in good agreement with previous literatures.[6,50] The partial current density of $J_{CO}$, calculated from CO FE and the total current density at a corresponding potential, is plotted in Fig. 2b. The $J_{CO}$ increased with reductive potential, suggesting a faster kinetic turnover of $CO_2$. At −1.1 V, $J_{CO}$ reached 12.4 mA $cm^{-2}$; with a similar trend, $J_{H_2}$ reached 7.0 mA $cm^{-2}$. Interestingly, the product ratio of $CO/H_2$ is approximately 2.5 for unmodified Au/C in the potential range of −0.7 to −1.1 V (Fig. 2c). Since both CO and $H_2$ are $2e^-$ reduction products, the selectivity of $CO_2$ over protons (or water) reduction is about 2.5 times on NHC-free AuNPs.

With polymer NHCs, the CO FE increased for all three catalysts. Au–P2 and Au–P3 showed similar CO FE of 85–95% at −0.7 to −1.1 V (Fig. 2g and j). Without hydrophobic PS, the CO FE of Au–P1 was around 80% (Fig. 2d), slightly lower than that of Au–P2 and Au–P3. The $J_{CO}$ also increased along with the hydrophobicity of polymer NHCs. At −1.1 V as an example, the $J_{CO}$ of Au–P1 was 16.1 ± 0.7 mA $cm^{-2}$; while, the $J_{CO}$ of Au–P2 and Au–P3 reached 21.2 ± 0.8 and 22.1 ± 0.9 mA $cm^{-2}$, close to 2-times higher than that of Au/C without NHC ligands. The $J_{H_2}$, however, did not follow the same trend. All polymer NHC ligands had a similar impact on $J_{H_2}$ and the decrease of $J_{H_2}$ was independent of polymer hydrophobicity. At −1.1 V, the $J_{H_2}$ of Au–P1, Au–P2 and Au–P3, was 4.2 ± 0.7, 3.4 ± 0.9 and 4.0 ± 0.9 mA $cm^{-2}$ respectively, that is about 50% of $J_{H_2}$ of pure Au. As a result, the product ratio of $CO/H_2$ increased with the hydrophobicity of polymers. At −0.9 V, the $CO/H_2$ ratio of Au–P1 is 5.5; and the $CO/H_2$ ratio of Au–P2 and Au–P3 is 8.1 and 8.5, respectively, that is about 3 times more selective to reduce $CO_2$ in comparison with Au/C. The role of polymer NHCs in $CO_2$ reduction, as we deducted from those results, is likely two-folded. First, polymer NHCs, regardless of their

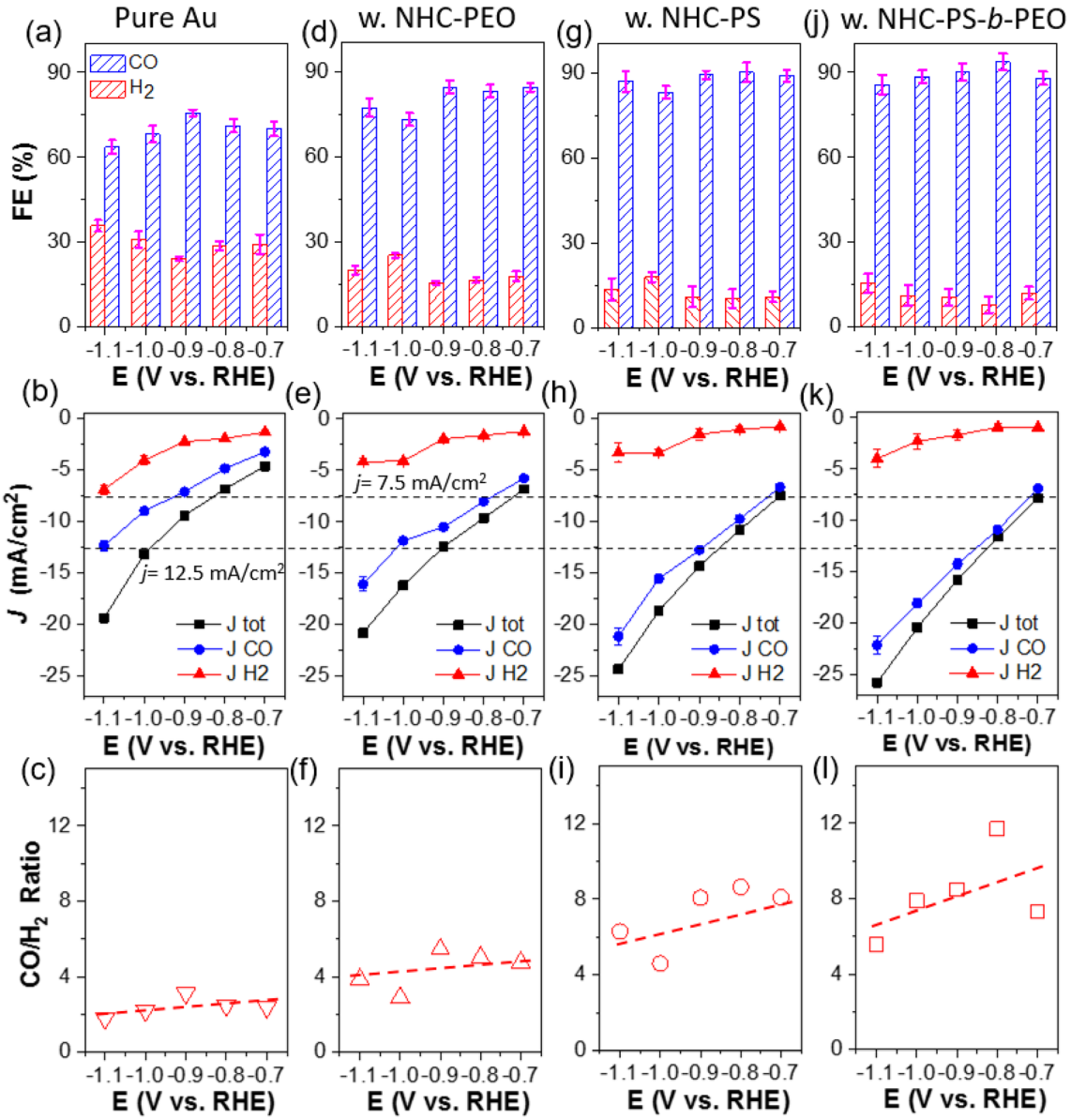


Fig. 2 Electrocatalytic performance of $CO_2$ reduction on different catalysts: FE, (partial) current density and product ratio (ordered vertically) using pure Au (a)–(c), Au–P1 (d)–(f), Au–P2 (g)–(i) and Au–P3 (j)–(l). All tests were carried out in $CO_2$ saturated 0.1 M $KHCO_3$.

hydrophobicity, would suppress the catalytic activity to reduce protons. The decrease of $J_{H_2}$ was seen in all three polymer ligands, although the grafting density and hydrophobicity of polymer ligands were different. Secondly, the hydrophobic PS would provide such a microenvironment to improve $CO_2$ selectivity and activity. When modifying Au/C with P1, the total current density ($J_{tot}$) did not show a noticeable increase but the $J_{H_2}$ had an obvious decrease. In the presence of hydrophobic PS, the increase of $J_{CO}$ (nearly no impact on $J_{H_2}$) suggests that the binding motif and polymer hydrophobicity likely play a very different role in $CO_2$ electroreduction. Furthermore, since the $J_{CO}$ as well as the $CO/H_2$ ratio of Au–P2 and Au–P3 were only marginally different, the PEO chains of amphiphilic P3 would have a minimum impact on $CO_2$ selectivity.

To distinguish the impact of polymers and the binding motif on the catalytic selectivity, AuNPs capped by the molecular NHC BMB–Im were examined for $CO_2$ electroreduction under identical conditions (Fig. 3a). The comparation of CO and $H_2$ FE are given in Fig. 3b and c. Interestingly, Au/C modified by BMB–Im showed very similar CO FE as Au–P1. This could also be confirmed through nearly identical $CO/H_2$ ratio close to 4 within same potential range (Fig. 3d). Both of them showed lower selectivity toward $H_2$ as compared to unmodified Au/C, suggesting that the NHC binding motif, instead of polymer chains, is responsible for the catalytic suppression of HER. Note that, Au modified by P1 had a higher activity as compared to that with BMB–Im (Fig. S8†). For the partial current density, the $J_{CO}$ of Au–P1 is 8.0 and 11.8 mA $cm^{-2}$ at −0.8 and −1.1 V, respectively (Fig. 3e), about 1.5-times higher than those of Au–

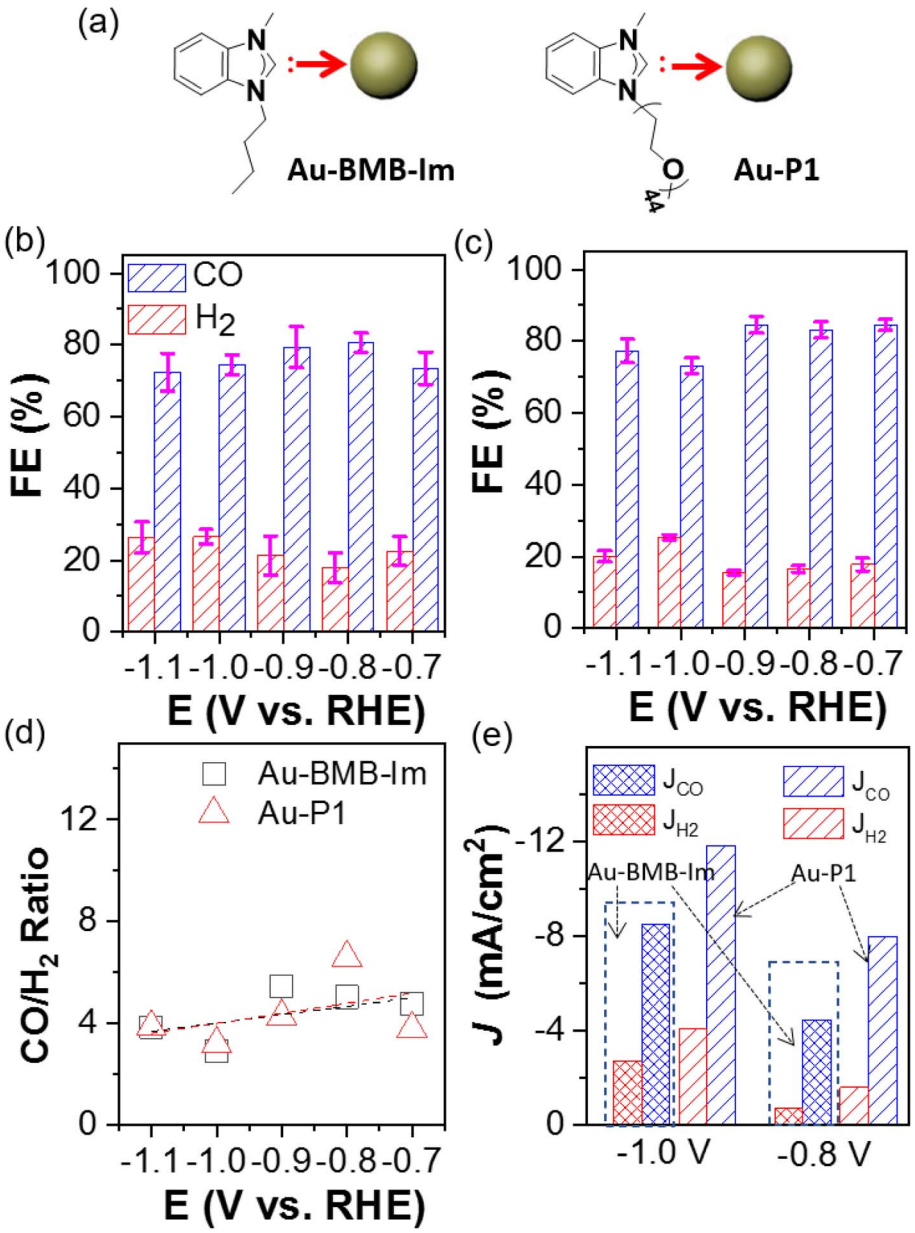


Fig. 3 (a) Scheme of BMB–Im and PEO–NHC modified AuNPs through Au–C binding. Catalytic selectivity to CO and $H_2$ using Au–BMB–Im (b) and Au–NHC–PEO (c). (d) Product ratio and (e) current density analysis of Au–BMB–Im and Au–NHC–PEO.

BMB–Im under the same potential. The activity toward HER shows a very similar trend. The higher activity for Au–P1 is likely due to the lower grafting density where the longer PEO chains would have much greater steric hindrance on the surface of AuNPs.

A number of previous studies have suggested the possible electronic perturbation of NHCs to surface atoms of NP catalysts.[39,51–53] NHCs bind with metal through the lone pair electrons on C; as a result, the σ donation of NHCs to the empty d orbitals of bound metal atoms would increase the electronic density of surface atoms of NP catalysts. As an electrophile, $CO_2$ favors the binding to electron-rich surface. Using *in situ* produced CO as a probe molecule, we used attenuated total reflectance surface-enhanced infrared absorption spectroscopy (ATR-SEIRAS) to measure the vibrational frequency of CO. A chemically deposited polycrystalline Au film upon reflecting Si prism was used as a working electrode. While Au has very weak binding with CO, the surface plasmon enhances the peak intensity significantly. At −0.3 V, the infrared spectra could be collected using the catalysts without bias as a background. In addition to the gaseous $CO_2$ peak centered at 2350 $cm^{-1}$, a new peak appeared at ~2120 $cm^{-1}$, assigned to the bound CO on the surface of Au (Fig. 4a and b).[54] After surface modification with P3 as an example, the bound CO shifted to 2108 $cm^{-1}$ (note the CO peak position is potential-dependent and it is compared at the same potential). As a π acceptor, CO with a lower stretching

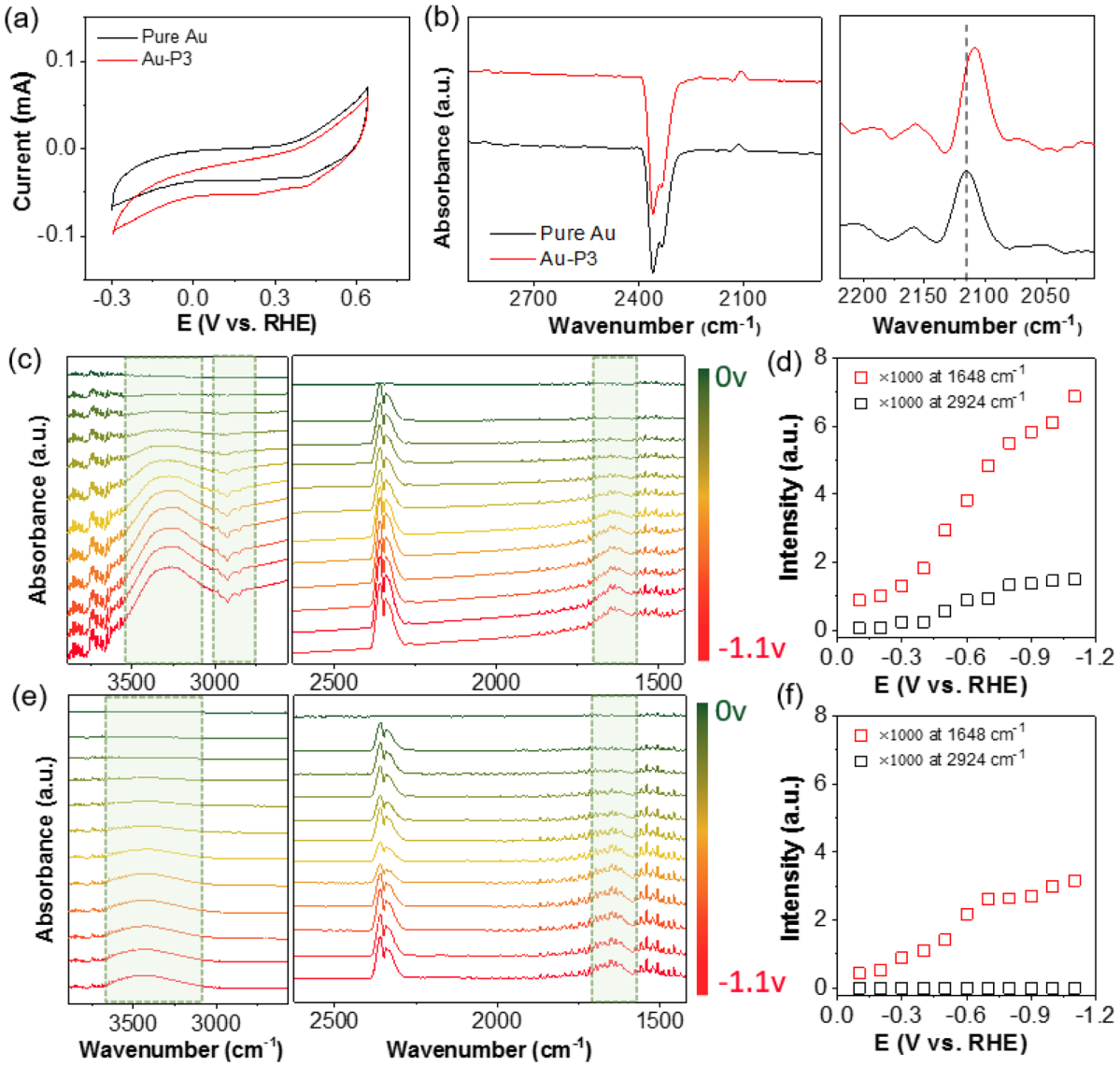


Fig. 4 Infrared spectroscopical study of Au electrodes with polymer NHC ligands. (a) CV scans in $N_2$ saturated 0.1 M $KHCO_3$ and (b) *in situ* ATR-SEIRAS spectra obtained at −0.3 $V_{RHE}$ of AuNPs and Au–NHC–PS-*b*-PEO, respectively. *In situ* ATR-SEIRAS spectra and vibrational peak intensity study for Au–NHC–PS-*b*-PEO (c) and (d) and pure AuNPs (e) and (f) in $CO_2$-purged 0.1 M $KHCO_3$ under various reductive potentials. The spectra in (c) and (e) are background subtracted at 0 V.

frequency indicates the electron-rich surface of AuNPs when modified with polymer NHCs. A high surface electron density through the σ-donation of NHCs likely favors $CO_2$ reduction over HER.[43,55,56] In addition, previous studies have demonstrated that NHCs potentially can stabilize the $CO_2$ adduct and intermediate $CO_2^{\bullet-}$ through hydrogen bonding,[57–59] also positively improving the selectivity for $CO_2$ reduction.

To gain more insights into the surface status at the electrode–electrolyte interface, especially in the presence of polymer NHCs, ATR-SEIRAS spectra were recorded on Au film electrodes during chronoamperometry scans under different potentials. Using the Au electrodes without bias as the background for all spectra, the positive peaks (pointing up) in the absorption model were from the yielded (or surface adsorbed) species during $CO_2$ electroreduction; while, the negative peaks (pointing down) arose from the desorbed species, *e.g.*, ligands. In Fig. 4e, the ATR-SEIRAS spectra on pure Au are given in the potential range of 0 to −1.1 V under constant-potential electrolysis. With the change of the negative bias, there were two positive peaks appeared, *e.g.*, a broad peak at 3300–3600 $cm^{-1}$ as the O–H stretching ($\nu_{O-H}$) and a well-defined peak at 1640 $cm^{-1}$ as the O–H bending ($\delta_{O-H}$). The $\nu_{O-H}$ peak centered at 3400 $cm^{-1}$ was broad as a typical characteristic for disordered water molecules. Those peak positions, along with the $CO_2$ doublet at 2361 and 2336 $cm^{-1}$,[60] agree very well the reported O–H vibrational frequency.[33,61,62] Fig. 4f shows the plot of the $\delta_{O-H}$ peak intensity as a function of potential. At around −0.3 V, there was a quick increase of the $\delta_{O-H}$ peak ($\nu_{O-H}$ in the similar trend), suggesting the re-orientation and adsorption of water as H-down on the electrode to couple with $CO_2$ reduction.[63] The

peak intensity saturated at around −0.8 V, known as the formation of densely packed layer of water for fast proton transfer.[61]

In the presence of polymer NHCs, the ATR-SEIRAS spectral features were obviously different. First, there was a large shift of the $\nu_{O-H}$ peak along with the peak sharpening (Fig. 4c). For Au–P3, the O–H stretching of adsorbed water downshifted to approximately 3300 $cm^{-1}$ with two shoulders at 3370 and 3247 $cm^{-1}$. In the absence of hydrophobic PS, Au–P1 and Au–BMB–Im do not show similar peak shift (Fig. S9†). The down shift of the $\nu_{O-H}$ peak indicates the formation of stronger hydrogen bonds of water, as compared to that without hydrophobic PS. This phenomena has been demonstrated in the phase transition of liquid water to ice.[64] In the presence of hydrophobic PS ligands, water molecules were likely confined at the electrode–electrolyte interface. With strong hydrogen bonding, water molecules form clusters presumably surrounded by hydrophobic ligands. Second, the peak intensity of adsorbed water showed a similar increased trend as that of unmodified Au; while, the peak intensity was much pronounced. The peak intensity was nearly doubled, and no saturation was observed in this case. Because the densely packed layer of water was only limited by the surface area of Au, it is likely that multiple layers of water were associated in Au–P3. Since strongly hydrogen bonded water did not show any peak shift with potential, re-orientated water was presumed to be stacked in the hydrophobic microenvironment. Lastly, negative peaks at 3100–2800 $cm^{-1}$ were seen at an onset potential of −0.5 V. Those peaks were assigned to the C–H bond stretching of $sp^2$ and $sp^3$ C of polymer backbones and side chains (also discussed in Fig. 8).[65] This was confirmed by the control of unmodified Au where no new peaks were observed in this region. We attributed those peaks to the dissociation of polymer NHCs from the electrode surface, although the peak intensity saturated quickly at −0.8 V (Fig. 4d).

Hydrophobic polymer NHCs as surface ligands were thought to alter the accessibility of Au in terms of the mass transfer during electrocatalysis. In view of $CO_2$ electroreduction as proton-coupled electron transfer, we further investigated whether the interface of hydrophobic polymers and Au would limit the diffusion of hydrated ions. Three different molecular probes were chosen to examine the interfacial mass transfer process during electrocatalysis. Specifically, the diffusive properties described by Randles–Ševčík equation can be determined by reversible redox under different scan rates, as described below:[66]

$$i_p = 0.4463nFAC_0\left(\frac{nFvD_0}{RT}\right)^{\frac{1}{2}}$$

where $n$ is the number of electrons in redox reaction, $F$ is Faraday's constant, $A$ is the electrode surface area, $C_0$ is the concentration of the electroactive species, $D_0$ is the diffusion coefficient of the electroactive species, and $v$ is the scan rate, respectively. Fig. 5a–c show the reversible redox behavior of the anionic probe, $K_3Fe(CN)_6$, on Au/C and Au–P3 in the range of 0.5 to 1.1 V with the scan rate from 40 to 100 mV $s^{-1}$. With the linear plot of the peak current ($I_p$) as a function of the square root of scan rate (Fig. 5c), the diffusion coefficient of $Fe(CN)_6^{3-}$ can be determined from the slope. As the diffusion of electroactive redox species to the Au surface can be limited by surface ligands, the measured $D_0$ could reflect the mass transfer status of ions at the interface of polymers and Au. Without polymer NHCs, the $D_0$ of ferricyanide anions is 1.7 × $10^{-6}$ $cm^2$ $s^{-1}$. It is

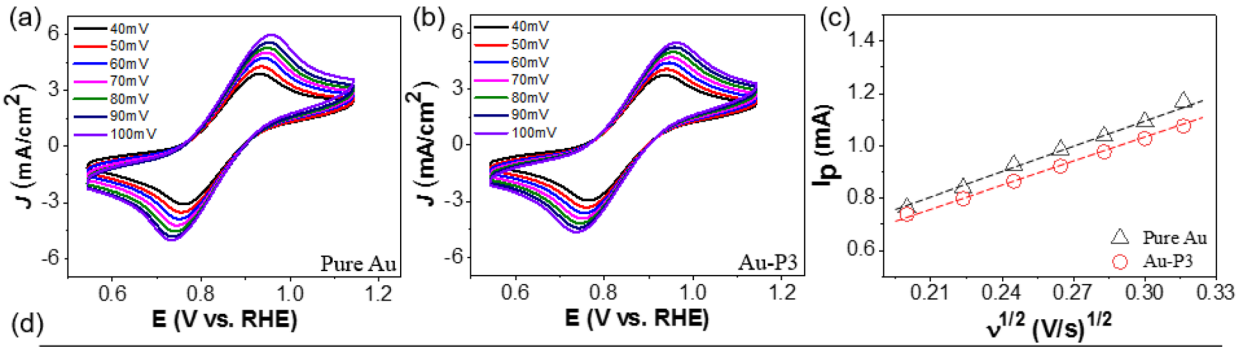


| Sample ID | $D_{Fe(CN)_6^{3-}}$ (×$10^{-6}$ $cm^2$ $s^{-1}$) | $D_{Ru(NH_3)_6^{3+}}$ (×$10^{-5}$ $cm^2$ $s^{-1}$) | $D_{Fc\text{-}COOH}$ (×$10^{-6}$ $cm^2$ $s^{-1}$) | $D_{CO_2}$ (×$10^{-9}$ $cm^2$ $s^{-1}$)[a] |
|---|---|---|---|---|
| Pure Au | 1.71±0.09 | 2.17±0.03 | 1.67±0.25 | 0.54 |
| Au-P1 | 1.00±0.03 | 1.72±0.15 | 3.09±0.40 | 0.29 |
| Au-P2 | 1.09±0.11 | 2.18±0.14 | 1.98±0.12 | 1.4 |
| Au-P3 | 1.23±0.04 | 1.33±0.02 | 3.47±0.12 | 1.4 |

[a]Note: $D_{CO_2}$ is from impedance spectroscopy.

Fig. 5 Interfacial diffusive properties of all catalysts. (a) CV scans of AuNPs and (b) Au–P3 measured with 50 mM $K_3Fe(CN)_6$ at various scan rates. (c) Linear relationship between peak current ($I_p$) and the square root of scan rates for pure Au and Au–P3. (d) Summary of diffusion coefficient ($D$) using various probe molecules including $Fe(CN)_6^{3-}$, $Ru(NH_3)_6^{3+}$, Fc–COOH, and $CO_2$.

close to the $D_0$ value for aqueous ferricyanide reported elsewhere.[67] In the presence of polymer NHCs, the $D_0$ decreased slightly to $1.0 \times 10^{-6}$, $1.1 \times 10^{-6}$, and $1.2 \times 10^{-6}$ cm$^2$ s$^{-1}$, for Au–P1, Au–P2 and Au–P3, respectively (Fig. S10†). Likewise, the diffusion coefficient of the cationic probe $Ru(NH_3)_6^{3+}$ showed a very similar trend (Fig. S11†). Despite a noticeable lower diffusion coefficient as compared to unmodified Au/C, the mass transfer of large ionic probes seems to be unrelated with the hydrophobicity of polymer NHCs. It is therefore reasonable to assume that the mass transport of small ions like protons would have a minimum change in the presence of hydrophobic polymer NHCs. This conclusion is in line with the partial current toward $H_2$ that is not correlated with the hydrophobicity or amphiphilicity of polymer NHCs.

More hydrophobic probes, like ferrocenecarboxylic acid (Fc–COOH), behave very differently from those strongly hydrated probes. Polymer NHCs did not slow down the diffusion of Fc–COOH. In case of Au–P1 and Au–P3, the measured $D_0$ of Fc–COOH was about 2-times higher than that of Au/C. The increase of $D_0$ of Fc–COOH is likely due to the hydrogen bonding of carboxylic acid and PEO (Fig. S12†). Unlike small molecular ligands that usually form a crystalline self-assembly monolayer,[68] the low grafting density of polymer ligands provides the diffusive channels to allow the redox reactions. For the $CO_2$ diffusion, electrochemical impedance spectroscopy (EIS) was used to fit the diffusion of $CO_2$ at −0.8 V over a frequency range of 100 kHz to 1 Hz (see Fig. S13 and details on data fitting in ESI†). The diffusion coefficient of $CO_2$ was close to $1.4 \times 10^{-9}$ cm$^2$ s$^{-1}$ for Au–P2 and Au–P3 with hydrophobic PS domain, that is about 3 times greater than that of Au/C. Although the diffusion coefficient from the impedance spectroscopy does not differ the diffusion of $CO_2$ from proton contribution from proton reduction was much smaller on Au catalysts modified by hydrophobic polymers (>90% CO FE). The increase of the diffusion coefficient of $CO_2$ should be responsible for the high selectivity for $CO_2$ over HER. Together with the SEIRAS results, one possible mechanism is that hydrophobic PS domains provide strong dehydration to $CO_2$ that allows faster conversion of $HCO_3^-$ ions to $CO_2$;[69] therefore, the local $CO_2$ concentration is higher than those without PS domains, similar to the $CO_2$ concentrating mechanism in photosynthesis. Therefore, hydrophobic polymer ligands would create a localized microenvironment that enriches $CO_2$ close to the active Au surface.

To investigate the effect of hydrophobic polymer ligands on the solvation structure around AuNPs, molecular dynamics (MD) simulations were carried out on a gold layer tethered with PS chains consisting of 66 repeating units (Fig. 6a). Fig. 6b shows the density profiles along the $z$ axis, perpendicular to the Au surface. At a surface coverage of 0.89 chains per nm$^2$, the polymer ligands created a sufficiently hydrophobic environment, with a clearly delineated bulk region at $z > 11.8$ nm and a water poor polymer layer for $z < 11.8$ nm. Yet, water peaks are

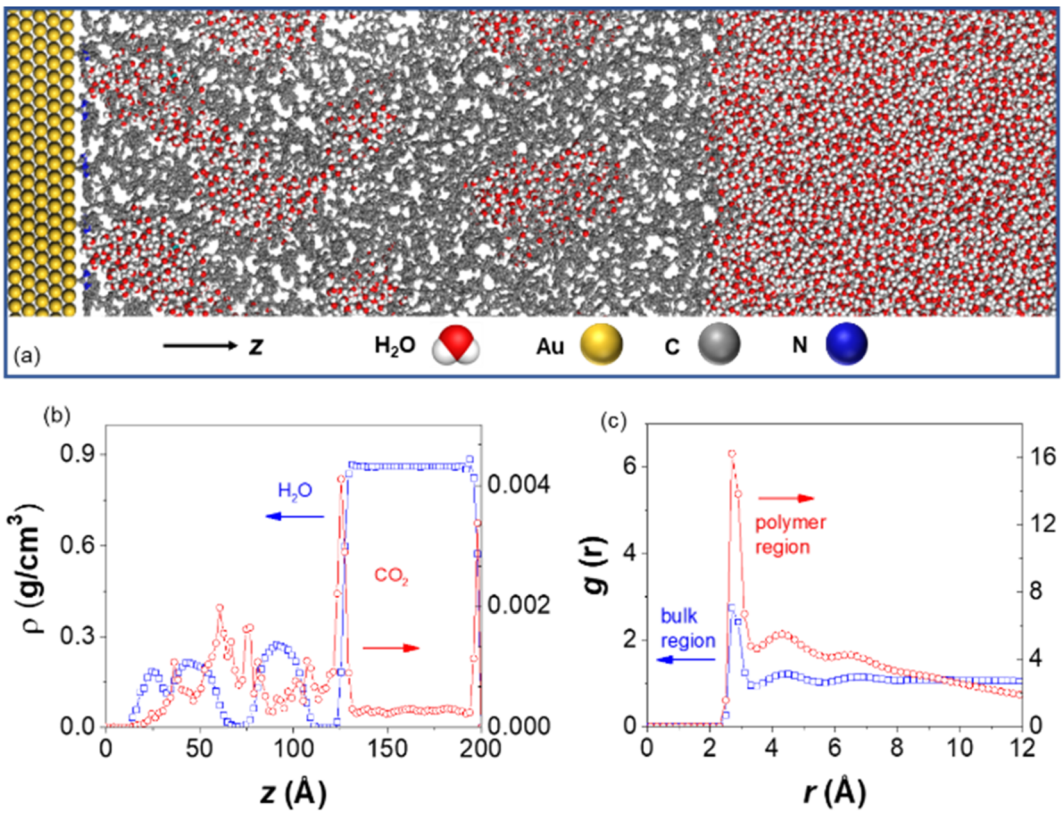


Fig. 6 (a) Illustration of the simulation setup, with the Au, C, N, O, H atoms represented in yellow, grey, blue, red, and white, respectively; (b) density profiles as a function of $z$ coordinates, with water and $CO_2$ shown in blue and red; (c) $O_w$–$O_w$ radial distribution function, analyzed for water molecules above $z = 11.8$ nm (bulk region, blue) and those below $z = 11.8$ nm (polymer layer, red).

found inside the polymer layer, corresponding to pockets of water embedded in hydrophobic PS. The differences in water structuring can be clearly identified in the oxygen–oxygen ($O_w$–$O_w$) radial distribution functions (RDFs) for water molecules in these two domains, as shown in Fig. 6c. While all RDFs show a first peak at $r = 0.28$ nm, as expected for bulk water, the peak heights are substantially different, with $g = 2.8$ for the bulk water region and $g = 16$ for the polymer layer. The first minimum and subsequent peak structures in the RDFs remain much higher than one, indicating strong aggregation but lack of longer-range order for water in the polymer region. Examining the simulation trajectories indicates that, despite the formation of localized water clusters, these clusters are dynamic and loosely connected to each other. Similar clustering is also confirmed with various $CO_2$ concentrations (Fig. S14†). Those results agree well with our experiments where dynamically clustered water was seen for AuNPs modified by hydrophobic PS. In addition, polymer chains effectively act as sorbent materials for $CO_2$ as suggested by its density profiles shown in Fig. 6b. There is a significantly higher density of $CO_2$ in the polymer layer than in the bulk water region, consistent with the increased $CO_2$ localized concentration and, therefore, reduction activity for polymer-modified AuNPs.

We finally investigated the electrochemical stability of Au catalysts to confirm the binding stability of polymer NHCs with Au surface. Fig. 7a shows the chronoamperometry ($i$–$t$) at −1.0 V. Without polymer NHCs, Au/C had a fast activity decay. The steady-state current decreased from −0.92 to −0.33 mA after electrolysis for 1 h, about 36% current retention. The current loss is attributed to the sintering of AuNPs under reductive potentials as confirmed by transmission electron microscopy (TEM, Fig. 7d). The fast aggregation and sintering of AuNPs as large as 50 nm were observed after 1 h, similar to the previous reports.[8] More quantitatively, the ECSA of AuNPs showed an 83% loss after electrolysis for 1 h at −1.0 V (Fig. 7c). In contrast, the electrocatalytic stability of AuNPs modified by all three polymers was greatly improved (Fig. 7b). The current retention was approximately 70%, regardless of the hydrophobicity of polymer NHCs (Fig. 7a). The ECSA of AuNPs agreed well with the activity retention; and the accessible surface area retention was 82.7%, 84.6% and 82% for Au–P1, Au–P2 and Au–P3, respectively (Fig. 7c). The steady-state current retention for Au–P2 and Au–P3 was approximately 80%. Fig. 7e shows the morphologic evolution of AuNPs capped by P3 (see Fig. S15† for more images). As confirmed by TEM images (Fig. 7e), AuNPs with polymer ligands showed structural integrity under electrolysis for 1 h at −1.0 V. The average size of Au–P3 is 15.6 ± 1.1 nm after electrolysis, close to their initial size of 14 ± 1.7 nm. Polymer NHCs work as a stabilization agent to prevent AuNPs from interparticle sintering, although there is a small decrease of activity. The measured stability of AuNPs modified by polymer NHCs is consistent with previous results on AuNPs and Pd/C.[9,43,70]

Since the ATR-SEIRAS results at different potential (see Fig. 4) suggested the possible removal of polymer NHCs under reductive potentials, the spectroscopic studies were further

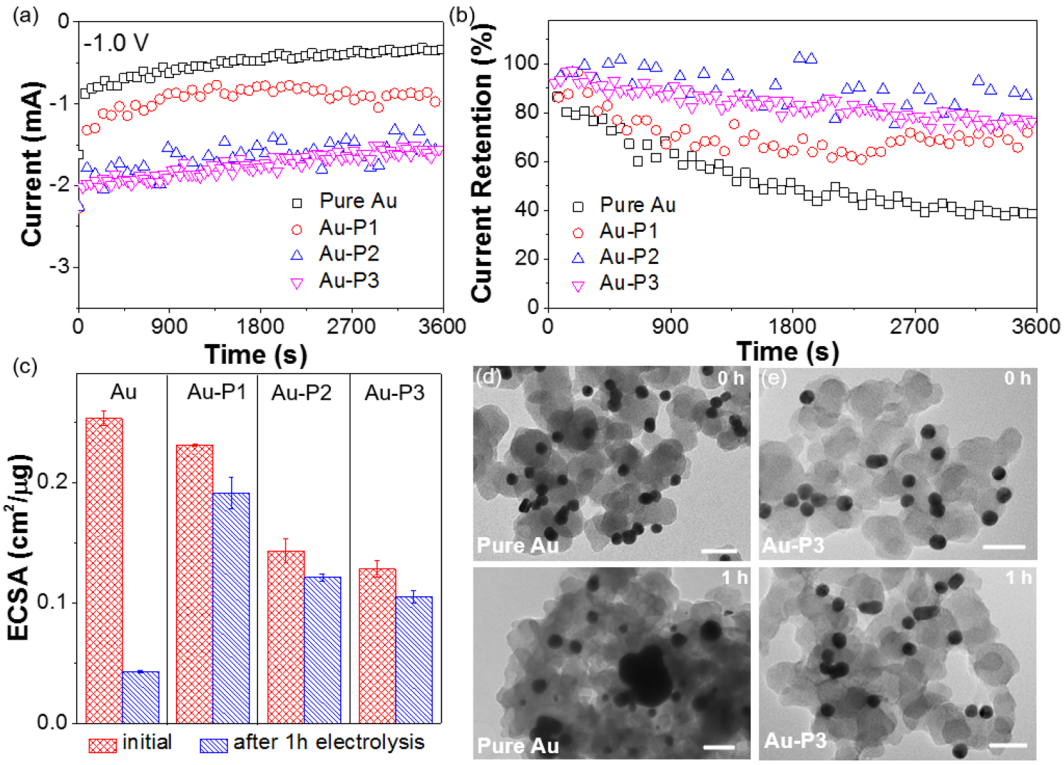


Fig. 7 Stability measurement using $i$–$t$ curves (a), current retention (b) and ECSA (c). The experiments were carried out using constant-potential electrolysis at −1.0 V for 1 h. TEM images of pure Au (d) and Au–P3 (e) loaded on carbon before (top) and after (bottom) $CO_2$ electroreduction for 1 h. All scale bars are 40 nm.

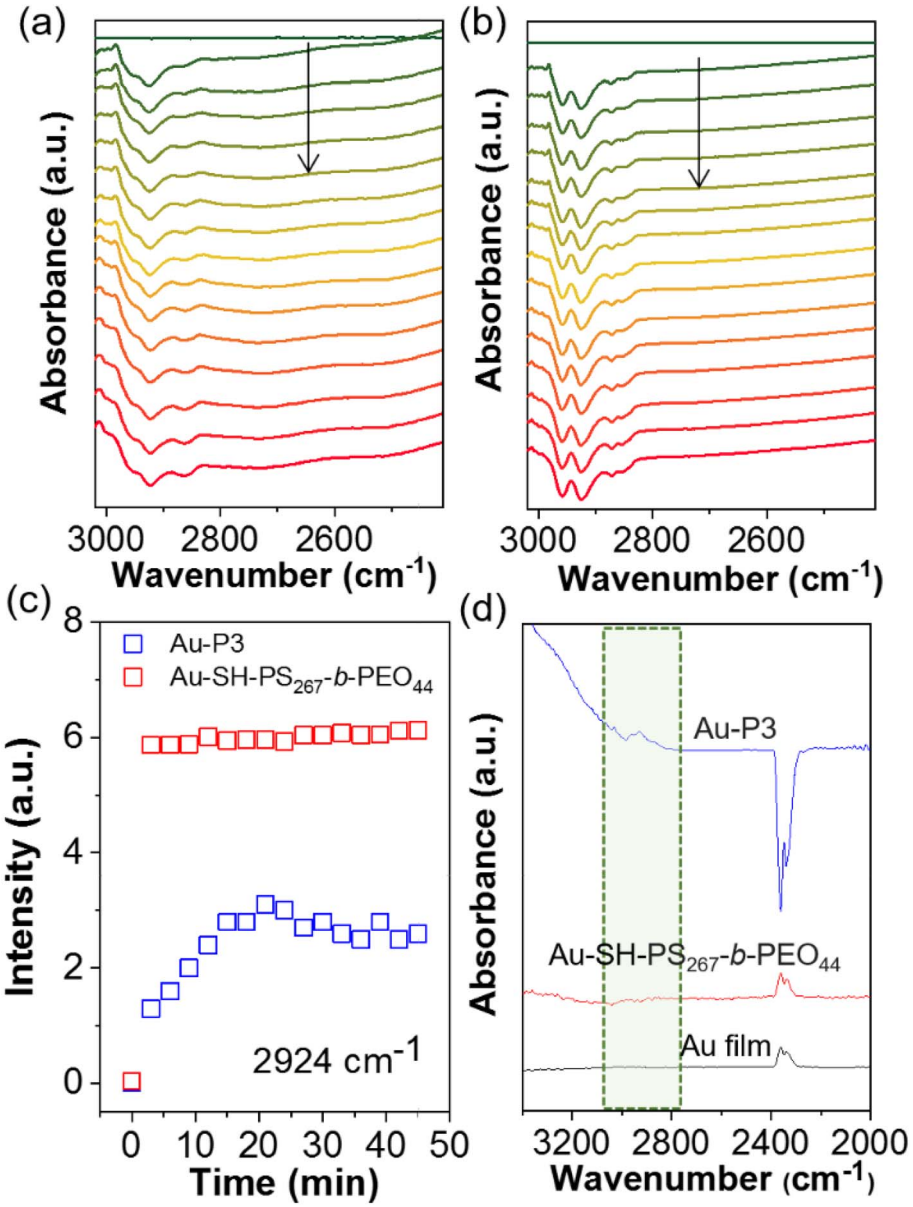


Fig. 8 *In situ* ATR-SEIRAS spectra of surface polymer modified electrode demonstrating the chemical stability of NHC ligands to counterpart thiol ligands. *In situ* ATR-SEIRAS spectra of (a) Au–NHC–PS-*b*-PEO and (b) Au–SH–$PS_{267}$-*b*-$PEO_{44}$ at −0.8 V on Au film electrode in $CO_2$ saturated 0.1 M $KHCO_3$ electrolyte. (c) The desorption vibrational peak intensity at 2924 $cm^{-1}$ against reaction time. (d) The adsorption peak intensity of different electrodes after electrocatalysis under −0.8 V. Blue: Au–P3, red: Au–SH; dark: Au film.

carried out to examine the electrochemical stability of polymer NHCs during $CO_2$ electroreduction. The *in situ* ATR-SEIRAS spectra were collected using constant-potential electrolysis. At −0.8 V, the spectra of Au modified by P3 were collected using the spectrum without bias as a background. Fig. 8a shows the desorption of polymer NHC. The negative peak appeared at ~2924 $cm^{-1}$ was assigned to the $sp^3$ C–H bond stretching, similar to the result under different potentials given in Fig. 4c. The peak intensity at 2924 $cm^{-1}$ as a function of time is, therefore, a measure of the desorption kinetics of NHCs on electrode surface (Fig. 8c). At first 20 min, there was a continuous increase of the peak intensity; and this trend saturated after 20 min. We measured the ATR-SEIRAS spectrum of the electrode after electrolysis for 45 min. There were clearly remaining polymer NHCs appeared at the same wavenumber (Fig. 8d). We assigned the initial surface desorption as the reconfiguration of polymer NHCs on the surface of the Au electrode. This could be due to the surface polarization under potential or the localized charge effect of Au surfaces.[71,72] Even though the quantification of ligand retention cannot be determined from this measurement, polymer NHCs with low grafting density could mostly stabilize NPs against sintering. As a control, we examined another thiol-terminated BCP of $PS_{267}$-*b*-$PEO_{44}$. Au–thiolate binding was unstable under $CO_2$ electroreduction as reported previously.[8,73] $PS_{267}$-*b*-$PEO_{44}$ had a similar spectral feature of surface desorption. However, it showed a fast

and burst desorption behavior (Fig. 8b). Those thiolate polymer ligands completely desorbed under bias. This could be confirmed by the spectrum collected after electrocatalysis for 45 min. A complete loss of thiolated polymers on Au was seen in the first 5 min. Those results suggested that Au–thiolate was not electrochemically stable under reductive conditions; and moreover, thiolate ligands did not provide the stability for AuNPs during $CO_2$ reduction as reported by Alivisatos[8] and others.[9]

## 3. Conclusion

In summary, we have successfully demonstrated the utilization of *N*-heterocyclic carbenes (NHCs) as a binding motif in conjunction with polymer hydrophobicity to exert control over substrate accessibility at the catalyst–electrolyte interface of gold nanoparticles (AuNPs) under redox conditions, as well as enhancing their long-term stability. Three distinct types of polymer ligands with different hydrophobicity/hydrophilicity were meticulously designed to modify AuNPs through NHC–Au binding. Irrespective of their hydrophobicity, AuNPs modified with polymer NHCs exhibited remarkable improvements in catalytic activity and selectivity. Notably, both homopolymer PS and PEO-*b*-PS NHCs, incorporating hydrophobic PS segments, exhibited a significant increase in selectivity for $CO_2$ reduction, achieving a remarkable CO faradaic efficiency of up to 95%. Moreover, the presence of any of the polymer NHCs led to a 50% reduction in the partial current density attributed to hydrogen formation. Importantly, the hydrophobic nature of the polymer ligands resulted in a twofold increase in the partial current density for CO formation compared to unmodified AuNPs or those modified with hydrophilic PEO. While all polymers did not impede ion diffusion, hydrophobic polymers appeared to influence the localized hydrogen bonding network of water, as evidenced by the outcomes of attenuated total reflectance surface-enhanced infrared absorption spectroscopy (ATR-SEIRAS) supertropical studies and MD simulations. Furthermore, the hydrophobic nature of polymer ligands clustered water molecules and facilitated an enrichment in the local $CO_2$ concentration, thereby enabling more efficient $CO_2$ reduction. Spectroelectrochemistry data obtained through ATR-SEIRAS suggested the relatively stable nature of the polymer NHC ligands under reductive conditions, as compared to thiol-terminated PS ligands. Collectively, our findings regarding the integration of robust NHC ligands with hydrophobic polymers provide valuable insights into the design of bioinspired hybrid catalysts for highly selective $CO_2$ reduction.

## Data availability

The datasets supporting this article have been uploaded as part of the ESI.†

## Author contributions

J. H. and S. S. designed and directed the project. Q. L., M. M., M. L., and K. W. carried out the $CO_2$ reduction experiments and spectroscopic studies. H. D. designed and synthesized all polymers. J. T. and P. B. planned and carried out the simulations. J. A. and G. U. designed the molecular carbenes. S. S. and S. L. S. did the TGA and XPS measurements. J. H. and Q. L. took the lead in writing the manuscript. All authors discussed the results and provided feedbacks on manuscript.

## Conflicts of interest

The authors declare that they have no conflict of interest.

## Acknowledgements

JH and SS is grateful for the financial support from the National Science Foundation (CHE 2102245 to JH and CHE-2102290 to Sun on experiments). PB acknowledges the support from the National Science Foundation (CBET 2144360 on simulation). The TEM images were obtained at the Biosciences Electron Microscopy Facility at the University of Connecticut. The computer simulations used resources of the National Energy Research Scientific Computing Center (NERSC) through allocation ERCAP0021594 and of the Advanced Cyberinfrastructure Coordination Ecosystem (ACCESS) through allocation CTS190069. This work was also partially supported by the Green Emulsions Micelles and Surfactants (GEMS) Center of the University of Connecticut.

## References

1 Z. Yin, G. T. R. Palmore and S. Sun, *Trends Chem.*, 2019, **1**, 739–750.
2 Z. Yin, J. Yu, Z. Xie, S.-W. Yu, L. Zhang, T. Akauola, J. G. Chen, W. Huang, L. Qi and S. Zhang, *J. Am. Chem. Soc.*, 2022, **144**, 20931–20938.
3 D. Gao, R. M. Arán-Ais, H. S. Jeon and B. Roldan Cuenya, *Nat. Catal.*, 2019, **2**, 198–210.
4 S. Li, A. V. Nagarajan, D. R. Alfonso, M. Sun, D. R. Kauffman, G. Mpourmpakis and R. Jin, *Angew. Chem., Int. Ed.*, 2021, **60**, 6351–6356.
5 S. Li, A. V. Nagarajan, X. Du, Y. Li, Z. Liu, D. R. Kauffman, G. Mpourmpakis and R. Jin, *Angew. Chem., Int. Ed.*, 2022, **61**, e202211771.
6 W. Zhu, R. Michalsky, Ö. Metin, H. Lv, S. Guo, C. J. Wright, X. Sun, A. A. Peterson and S. Sun, *J. Am. Chem. Soc.*, 2013, **135**, 16833–16836.
7 C. Rogers, W. S. Perkins, G. Veber, T. E. Williams, R. R. Cloke and F. R. Fischer, *J. Am. Chem. Soc.*, 2017, **139**, 4052–4061.
8 K. Manthiram, Y. Surendranath and A. P. Alivisatos, *J. Am. Chem. Soc.*, 2014, **136**, 7237–7240.
9 L. Zhang, Z. Wei, S. Thanneeru, M. Meng, M. Kruzyk, G. Ung, B. Liu and J. He, *Angew. Chem., Int. Ed.*, 2019, **58**, 15834–15840.
10 J. Huang, N. Hörmann, E. Oveisi, A. Loiudice, G. L. De Gregorio, O. Andreussi, N. Marzari and R. Buonsanti, *Nat. Commun.*, 2018, **9**, 3117.
11 P. Grosse, A. Yoon, C. Rettenmaier, A. Herzog, S. W. Chee and B. Roldan Cuenya, *Nat. Commun.*, 2021, **12**, 6736.

12 V. Okatenko, A. Loiudice, M. A. Newton, D. C. Stoian, A. Blokhina, A. N. Chen, K. Rossi and R. Buonsanti, *J. Am. Chem. Soc.*, 2023, **145**, 5370–5383.
13 S. Zhao, R. Jin and R. Jin, *ACS Energy Lett.*, 2018, **3**, 452–462.
14 A. Wadas, A. Gorczynski, I. A. Rutkowska, E. Seta-Wiaderek, E. Szaniawska, M. Kubicki, A. Lewera, M. Gorzkowski, A. Januszewska, R. Jurczakowski, B. Palys, V. Patroniak and P. J. Kulesza, *Electrochim. Acta*, 2021, **388**, 138550.
15 A. Goyal, G. Marcandalli, V. A. Mints and M. T. M. Koper, *J. Am. Chem. Soc.*, 2020, **142**, 4154–4161.
16 C. W. Li and M. W. Kanan, *J. Am. Chem. Soc.*, 2012, **134**, 7231–7234.
17 X. Su, Y. Sun, L. Jin, L. Zhang, Y. Yang, P. Kerns, B. Liu, S. Li and J. He, *Appl. Catal., B*, 2020, **269**, 118800.
18 D. Gao, H. Zhou, J. Wang, S. Miao, F. Yang, G. Wang, J. Wang and X. Bao, *J. Am. Chem. Soc.*, 2015, **137**, 4288–4291.
19 F. Cai, D. Gao, H. Zhou, G. Wang, T. He, H. Gong, S. Miao, F. Yang, J. Wang and X. Bao, *Chem. Sci.*, 2017, **8**, 2569–2573.
20 J.-H. Kim, H. Woo, J. Choi, H.-W. Jung and Y.-T. Kim, *ACS Catal.*, 2017, **7**, 2101–2106.
21 L.-P. Yuan, W.-J. Jiang, X.-L. Liu, Y.-H. He, C. He, T. Tang, J. Zhang and J.-S. Hu, *ACS Catal.*, 2020, **10**, 13227–13235.
22 L. Jin, B. Liu, P. Wang, H. Yao, L. A. Achola, P. Kerns, A. Lopes, Y. Yang, J. Ho, A. Moewes, Y. Pei and J. He, *Nanoscale*, 2018, **10**, 14678–14686.
23 C. W. Lee, S.-J. Shin, H. Jung, D. L. T. Nguyen, S. Y. Lee, W. H. Lee, D. H. Won, M. G. Kim, H.-S. Oh, T. Jang, H. Kim, B. K. Min and Y. J. Hwang, *ACS Energy Lett.*, 2019, **4**, 2241–2248.
24 C. Janáky, D. Hursán, B. Endrődi, W. Chanmanee, D. Roy, D. Liu, N. R. de Tacconi, B. H. Dennis and K. Rajeshwar, *ACS Energy Lett.*, 2016, **1**, 332–338.
25 S. Huo, Z. Weng, Z. Wu, Y. Zhong, Y. Wu, J. Fang and H. Wang, *ACS Appl. Mater. Interfaces*, 2017, **9**, 28519–28526.
26 X. Zhou, H. Liu, B. Y. Xia, K. Ostrikov, Y. Zheng and S.-Z. Qiao, *SmartMat*, 2022, **3**, 111–129.
27 D. Kim, S. Yu, F. Zheng, I. Roh, Y. Li, S. Louisia, Z. Qi, G. A. Somorjai, H. Frei, L.-W. Wang and P. Yang, *Nat. Energy*, 2020, **5**, 1032–1042.
28 Q. Zhu, C. J. Murphy and L. R. Baker, *J. Am. Chem. Soc.*, 2022, **144**, 2829–2840.
29 L. Lu, S. Zou and B. Fang, *ACS Catal.*, 2021, **11**, 6020–6058.
30 H. Shang, S. K. Wallentine, D. M. Hofmann, Q. Zhu, C. J. Murphy and L. R. Baker, *Chem. Sci.*, 2020, **11**, 12298–12306.
31 Z. Wang, L. Wu, K. Sun, T. Chen, Z. Jiang, T. Cheng and W. A. Goddard III, *J. Phys. Chem. Lett.*, 2018, **9**, 3057–3061.
32 J. R. Pankhurst, P. Iyengar, A. Loiudice, M. Mensi and R. Buonsanti, *Chem. Sci.*, 2020, **11**, 9296–9302.
33 W. Ge, Y. Chen, Y. Fan, Y. Zhu, H. Liu, L. Song, Z. Liu, C. Lian, H. Jiang and C. Li, *J. Am. Chem. Soc.*, 2022, **144**, 6613–6622.
34 S. Sun, *Nat. Energy*, 2020, **5**, 943–944.
35 L. Jin, B. Liu, S. S. Duay and J. He, *Catalysts*, 2017, **7**, 44.
36 K. Wei, H. Guan, Q. Luo, J. He and S. Sun, *Nanoscale*, 2022, **14**, 11869–11891.
37 F. P. García de Arquer, C.-T. Dinh, A. Ozden, J. Wicks, C. McCallum, A. R. Kirmani, D.-H. Nam, C. Gabardo, A. Seifitokaldani, X. Wang, Y. C. Li, F. Li, J. Edwards, L. J. Richter, S. J. Thorpe, D. Sinton and E. H. Sargent, *Science*, 2020, **367**, 661–666.
38 D. Wakerley, S. Lamaison, F. Ozanam, N. Menguy, D. Mercier, P. Marcus, M. Fontecave and V. Mougel, *Nat. Mater.*, 2019, **18**, 1222–1227.
39 C. A. Smith, M. R. Narouz, P. A. Lummis, I. Singh, A. Nazemi, C.-H. Li and C. M. Crudden, *Chem. Rev.*, 2019, **119**, 4986–5056.
40 C. Richter, K. Schaepe, F. Glorius and B. J. Ravoo, *Chem. Commun.*, 2014, **50**, 3204–3207.
41 C. Eisen, J. M. Chin and M. R. Reithofer, *Chem.–Asian J.*, 2021, **16**, 3026–3037.
42 Y. Jiang, Y. Yu, X. Zhang, M. Weinert, X. Song, J. Ai, L. Han and H. Fei, *Angew. Chem., Int. Ed.*, 2021, **60**, 17388–17393.
43 Z. Cao, J. S. Derrick, J. Xu, R. Gao, M. Gong, E. M. Nichols, P. T. Smith, X. Liu, X. Wen, C. Copéret and C. J. Chang, *Angew. Chem., Int. Ed.*, 2018, **57**, 4981–4985.
44 L. Zhang, Z. Wei, M. Meng, G. Ung and J. He, *J. Mater. Chem. A*, 2020, **8**, 15900–15908.
45 Z. Wei, M. Kayceety, A. Price, K. Wei, Q. Luo, S. Thanneeru, S. Sun and J. He, *ACS Appl. Mater. Interfaces*, 2022, **14**, 55227–55237.
46 H. Duan, Y. Lin and J. He, in *World Scientific Reference on Plasmonic Nanomaterials: Principles, Design and Bio-applications: Volume 3: Self-Assembly of Plasmonic Nanostructures*, World Scientific, 2022, pp. 409–432.
47 G. H. Gunasekar, K. Park, V. Ganesan, K. Lee, N.-K. Kim, K.-D. Jung and S. Yoon, *Chem. Mater.*, 2017, **29**, 6740–6748.
48 N. Bridonneau, L. Hippolyte, D. Mercier, D. Portehault, M. Desage-El Murr, P. Marcus, L. Fensterbank, C. Chanéac and F. Ribot, *Dalton Trans.*, 2018, **47**, 6850–6859.
49 Y. H. Tan, J. A. Davis, K. Fujikawa, N. V. Ganesh, A. V. Demchenko and K. J. Stine, *J. Mater. Chem.*, 2012, **22**, 6733–6745.
50 H.-E. Lee, K. D. Yang, S. M. Yoon, H.-Y. Ahn, Y. Y. Lee, H. Chang, D. H. Jeong, Y.-S. Lee, M. Y. Kim and K. T. Nam, *ACS Nano*, 2015, **9**, 8384–8393.
51 A. Rühling, K. Schaepe, L. Rakers, B. Vonhören, P. Tegeder, B. J. Ravoo and F. Glorius, *Angew. Chem., Int. Ed.*, 2016, **55**, 5856–5860.
52 J. B. Ernst, C. Schwermann, G.-i. Yokota, M. Tada, S. Muratsugu, N. L. Doltsinis and F. Glorius, *J. Am. Chem. Soc.*, 2017, **139**, 9144–9147.
53 M. N. Hopkinson, C. Richter, M. Schedler and F. Glorius, *Nature*, 2014, **510**, 485–496.
54 Y. Katayama, F. Nattino, L. Giordano, J. Hwang, R. R. Rao, O. Andreussi, N. Marzari and Y. Shao-Horn, *J. Phys. Chem. C*, 2019, **123**, 5951–5963.
55 Z. Cao, D. Kim, D. Hong, Y. Yu, J. Xu, S. Lin, X. Wen, E. M. Nichols, K. Jeong, J. A. Reimer, P. Yang and C. J. Chang, *J. Am. Chem. Soc.*, 2016, **138**, 8120–8125.
56 G. Chen, C. Xu, X. Huang, J. Ye, L. Gu, G. Li, Z. Tang, B. Wu, H. Yang, Z. Zhao, Z. Zhou, G. Fu and N. Zheng, *Nat. Mater.*, 2016, **15**, 564–569.

57 S. Neyrizi, J. Kiewiet, M. A. Hempenius and G. Mul, *ACS Energy Lett.*, 2022, **7**, 3439–3446.
58 X. Li and J. A. Panetier, *Phys. Chem. Chem. Phys.*, 2021, **23**, 14940–14951.
59 G. P. S. Lau, M. Schreier, D. Vasilyev, R. Scopelliti, M. Grätzel and P. J. Dyson, *J. Am. Chem. Soc.*, 2016, **138**, 7820–7823.
60 A. L. Goodman, L. M. Campus and K. T. Schroeder, *Energy Fuels*, 2005, **19**, 471–476.
61 E. R. Corson, R. Kas, R. Kostecki, J. J. Urban, W. A. Smith, B. D. McCloskey and R. Kortlever, *J. Am. Chem. Soc.*, 2020, **142**, 11750–11762.
62 S. Zhu, T. Li, W.-B. Cai and M. Shao, *ACS Energy Lett.*, 2019, **4**, 682–689.
63 Z. D. Schultz, S. K. Shaw and A. A. Gewirth, *J. Am. Chem. Soc.*, 2005, **127**, 15916–15922.
64 S. Le Caër, G. Klein, D. Ortiz, M. Lima, S. Devineau, S. Pin, J. B. Brubach, P. Roy, S. Pommeret, W. Leibl, R. Righini and J. P. Renault, *Phys. Chem. Chem. Phys.*, 2014, **16**, 22841–22852.
65 D. S. Ramadhan, Warsito and E. D. Iftitah, *IOP Conf. Ser.: Mater. Sci. Eng.*, 2018, **299**, 012076.
66 C. Sandford, M. A. Edwards, K. J. Klunder, D. P. Hickey, M. Li, K. Barman, M. S. Sigman, H. S. White and S. D. Minteer, *Chem. Sci.*, 2019, **10**, 6404–6422.
67 J. Moldenhauer, M. Meier and D. W. Paul, *J. Electrochem. Soc.*, 2016, **163**, H672.
68 S. T. Marshall, M. O'Brien, B. Oetter, A. Corpuz, R. M. Richards, D. K. Schwartz and J. W. Medlin, *Nat. Mater.*, 2010, **9**, 853–858.
69 A. Stirling, *J. Phys. Chem. B*, 2011, **115**, 14683–14687.
70 J. A. Trindell, J. Clausmeyer and R. M. Crooks, *J. Am. Chem. Soc.*, 2017, **139**, 16161–16167.
71 S. E. Weitzner, S. A. Akhade, J. B. Varley, B. C. Wood, M. Otani, S. E. Baker and E. B. Duoss, *J. Phys. Chem. Lett.*, 2020, **11**, 4113–4118.
72 H. Tsunoyama, N. Ichikuni, H. Sakurai and T. Tsukuda, *J. Am. Chem. Soc.*, 2009, **131**, 7086–7093.
73 Y. Sato and F. Mizutani, *Phys. Chem. Chem. Phys.*, 2004, **6**, 1328–1331.